

A new interpretation for the nature and significance of mirror-like
surfaces in experimental carbonate-hosted seismic faults:

Supplementary material

Giacomo Pozzi^{1*}, Nicola De Paola¹, Stefan B. Nielsen¹, Robert E. Holdsworth¹, Leon Bowen²,

¹*Department of Earth Sciences, Rock Mechanics Laboratory, Durham University, South road,*

*Durham, DH1 3LE, UK. *(giacomo.pozzi@durham.ac.uk)*

²*Department of Physics, Durham University, Durham, DH1 3LE, UK.*

DR1: Sample assembly

A sample assembly with hollow geometry is used and consists of two cylinders of titanium-vanadium alloy (Ti90Al6V4, Yao et al., 2016), external radius of 12.5 mm and inner radius of 5.25 mm, sandwiching a layer of gouge. One base of both cylinders is machined with a crosshatch pattern of grooves (500 μm deep), which forces the shear localization in the gouge. An inner Teflon cylinder and an outer Teflon ring, which is tightly fastened to the cylinder by a hose clip, are mounted on the lower cylinder to prevent the internal and lateral extrusion of the gouge, respectively. The Teflon ring has a smaller inner radius (~ 12.4) than the cylinders to ensure a tight fit. 1 g of gouge is carefully poured in the annular chamber formed on the bottom cylinder, which is gently tapped to achieve a uniform thickness of the gouge sample. The initial thickness (~ 1.4 mm) is checked with a caliper to attest the reproducibility of the preparation. The top cylinder is mounted directly on the rotating shaft of the machine and carefully centered (± 5 μm) to avoid axial misalignment. The assembled bottom cylinder is mounted on the lower column, where the torque and axial load gages and the vertical displacement transducer are mounted (further information about the apparatus can be found in De Paola et al., 2015, Supplementary Information I). A pneumatic cylinder installed at the bottom of the lower column is used to apply the normal force on the sample up to 10 kN. Maximum force integrated over the hollow cylinder gives a normal pressure of ~ 25 MPa.

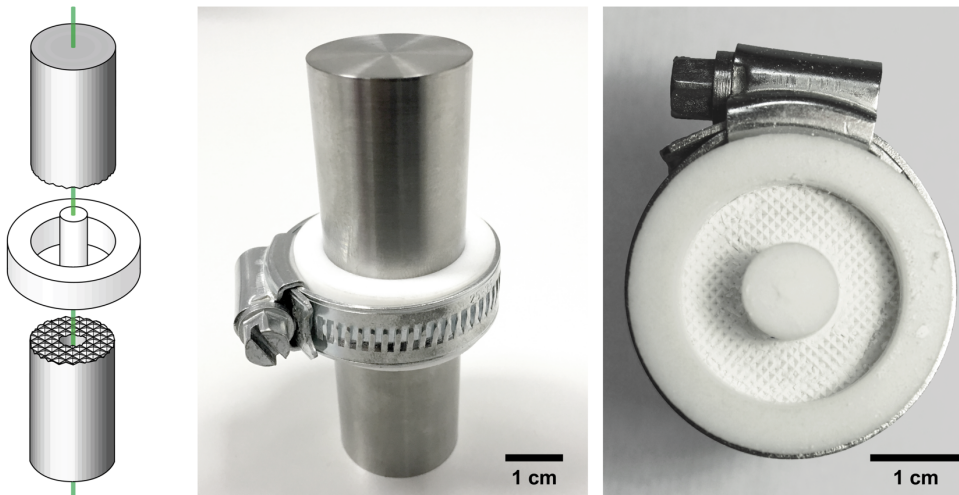


Figure DR1: Cylinder assembly (from left to right): schematic representation of the mount, lateral view of the sealed annular chamber, top view of the annular chamber containing calcite gouge (teeth marks are visible on top).

References in DR1.

Yao, L., Ma, S., Platt, J.D., Niemeijer, A.R., and Shimamoto, T., 2016, The crucial role of temperature in high-velocity weakening of faults: Experiments on gouge using host blocks with different thermal conductivities: *Geology*, v. 44, p. 63–66.

DR2: Temperature estimate

A simple monodimensional equation for heat diffusion in a half space from a thin tabular source is utilised to estimate the temperature rise (ΔT) in the principal slip zone (PSZ; Carslaw and Jaeger, 1986; Rice, 2006):

$$\Delta T(t) = \frac{1}{\rho c_p \sqrt{\pi \kappa}} \int_0^t \frac{\Phi(t')}{\sqrt{t-t'}} \exp\left(-\frac{W^2}{4\kappa(t-t')}\right) dt' \quad (1)$$

where ρ is the density, c_p is the specific heat, κ is the thermal diffusivity, Φ is the heat flux, t is time and W is the PSZ thickness (m)

This equation does not consider heat sinks apart from heat diffusion from the shear zone.

When the following relation is satisfied

$$W \ll 4\sqrt{(\kappa\delta/v)} \quad (2)$$

where δ is the displacement and v is the slip rate (m/s), W is negligible compared to the time scale of heat diffusion and

$$\exp\left(-\frac{W^2}{4\kappa(t-t')}\right) \approx 1 \quad (3)$$

In this case, Equation 1 may be simplified to the following non adiabatic case

$$\Delta T(t) = \frac{1}{\rho c_P \sqrt{\pi\kappa}} \int_0^t \frac{\Phi(t')}{\sqrt{t-t'}} dt' \quad (4)$$

The heat flux radiating through one of the boundaries of the brittle shear band can be calculated by (Rice, 2006)

$$\Phi(t) = \frac{\tau(t)v}{2} = \frac{\mu(t)\sigma_n v}{2} \quad (5)$$

where τ is the shear stress, σ_n is the normal stress and μ is the friction coefficient, to obtain

$$\Delta T = \frac{v}{2\rho c_P \sqrt{\pi\kappa}} \int_0^t \frac{\tau(t')}{\sqrt{t-t'}} dt' = \frac{\sigma_n v}{2\rho c_P \sqrt{\pi\kappa}} \int_0^t \frac{\mu(t')}{\sqrt{t-t'}} dt' \quad (6)$$

It is important to note that the temperature rise calculated by Equation 6 is an upper estimate, as no other heat sinks are accounted for apart from heat diffusion. In fact, as reported in the main text, we argue that all of the deformation energy in the deforming slip zone is dissipated as heat and that decarbonation reactions were not quantitatively significant. For the scope of the paper, the temperature values obtained are used as a first approximation of the thermal conditions during the weakening process.

References in DR2.

Carslaw, H.S., and Jaeger, J.C., 1986, *Conduction Of Heat In Solids*: Oxford Oxfordshire : New York, Oxford University Press, U.S.A.

Rice, J.R., 2006, Heating and weakening of faults during earthquake slip: *Journal of Geophysical Research: Solid Earth*, v. 111, p. B05311.

DR3: Mechanical data

The mechanical data discussed in this paper are summarised in Table 1 and the experimental results are plotted in Figures 3-5. All of the experiments have been run for displacements up to 1 m at the reference radius (8.97 rotations). However, experiments run at low velocities ($v < 0.3 \text{ ms}^{-1}$) frequently failed after a certain amount of slip due to gouge loss (shown by * in Table 1). For these experiments, only the reliable part of each run is plotted in Figures 3-5 and its total displacement is reported in table 1.

Shear stress curves have been fitted using the exponential decay equation (Fig. DR2B):

$$\tau_f = \tau_{SS} + (\tau_P - \tau_{SS})e^{\left[\frac{\ln(\alpha)\delta}{D_W}\right]} \quad (7)$$

where τ_f is the fitted shear stress, τ_{SS} and τ_P are the shear stress at steady state and peak conditions, respectively, α is a best fit coefficient, δ is the displacement and D_W is the slip weakening distance (modified after Mizoguchi *et al.*, 2007 and De Paola *et al.*, 2011). D_W is calculated as the displacement required for the shear stress to decrease from τ_P by an amount equal to 95% of $(\tau_P - \tau_{SS})$. The values used in the calculation are reported in Table 1.

Table 1

Exp. #	v (ms^{-1})	δ (m)	δ_{tr} (cm)	σ_n (MPa)	τ_p (MPa)	τ_{ss} (MPa)	μ_{ss}	D_c (m)	α	T_W ($^{\circ}\text{C}$)
VF 666	1.4 E+0	0.04	4.7	25.0	20.1	3.8	0.15	0.4	1E-11	751
VF 664		0.07								
VF 695		0.26								
VF 662		0.26								
VF 693		0.26								
VF 660		0.90								
VF 793		3.24								
VF 827	5.8 E-1	1.00	4.7	25.0	21.2	5.6	0.22	0.31	5E-9	735
VF 828	3.6 E-1	1.00	4.7	25.0	20.1	6.8	0.27	0.25	3E-8	604
VF 829*	2.5 E-1	0.60	4.7	25.0	20.0	~8.6	~0.34	~0.23	2E-6	487
VF 680	1.4 E-1	0.08	6.4	25.0	21.4	~10.5	~0.42	~0.25	3E-5	474
VF 675		0.23								
VF 679*		0.26								
VF 677*		0.29								
VF 676*		0.37								
VF 803*		0.39								
VF 834*	7.7 E-2	0.15	9	25.0	-	-	-	-	-	445
VF 831*	4.6 E-2	0.20	12	25.0	-	-	-	-	-	410
VF 833*	3.1 E-2	0.22	20	25.0	-	-	-	-	-	420
VF 672*	1.4 E-2	0.13	27	25.0	-	-	-	-	-	334
VF 673*		0.18								
VF 824*		0.32								
VF 670	1.4 E-3	0.07	-	25.0	-	-	-	-	-	-
VF 823*		0.32	-	-	-	-	-	-	-	-

Table 1: Compendium of mechanical data where v is the slip rate, δ is the total displacement for the reliable part of the experiment, δ_{tr} is the displacement to the onset of weakening (stage II in experiments with $v > 0.077 \text{ ms}^{-1}$), σ_n is the normal stress, τ_p is the peak shear stress (end of stage I), τ_{ss} is the shear stress at (quasi-) steady state conditions, μ_{ss} is the friction coefficient at (quasi-) steady state conditions, D_c is the weakening distance, α is a best-fit coefficient used in Equation 7 and T_W is the calculated PSZ bulk temperature at the onset of weakening (room $T = 25^{\circ}\text{C}$).

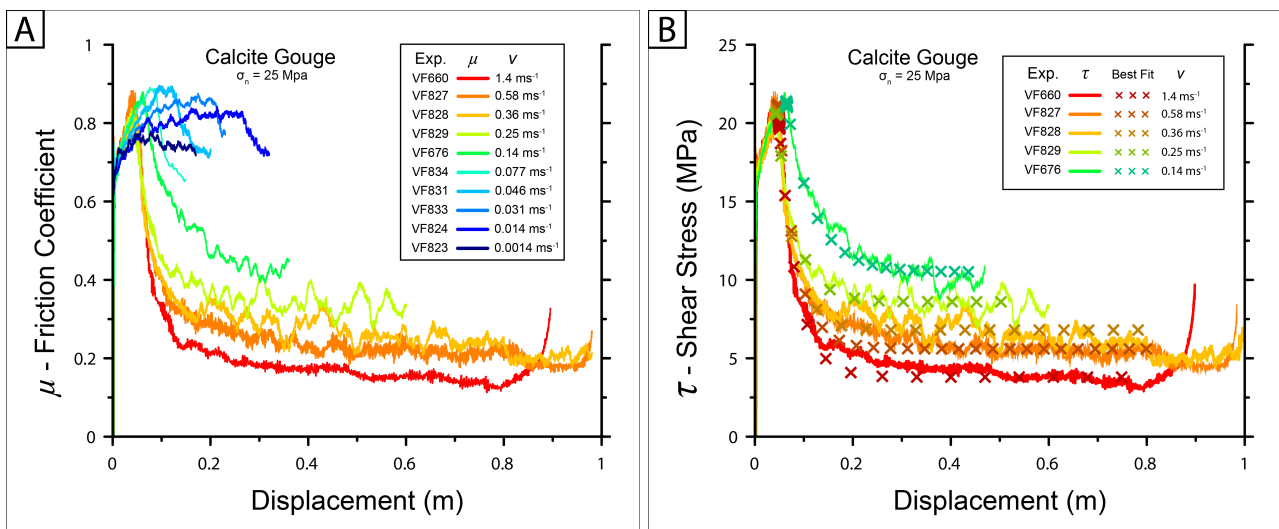


Figure DR2: Representative friction coefficient (A) and shear stress (B) curves plotted over displacement for different velocities (with $\sigma_n = 25 \text{ MPa}$). Best fit curves calculated with Equation 7 using the variables reported in Table 1 are plotted with X symbols in B). Onset of weakening and (quasi-) steady state (stage III) friction coefficient are clearly slip rate dependent.

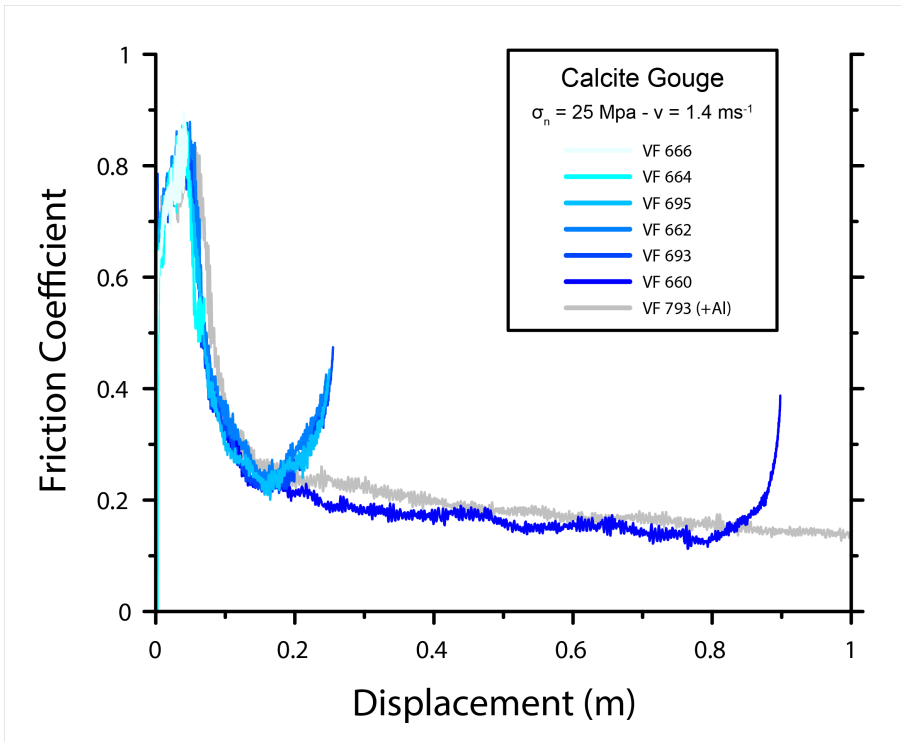


Figure DR3: Friction coefficient curves plotted over displacement for experiments performed at slip rate of 1.4 ms^{-1} . VF_793 shows a slightly different behaviour due to the contamination with low amounts of Al_2O_3 powder, used as strain marker.

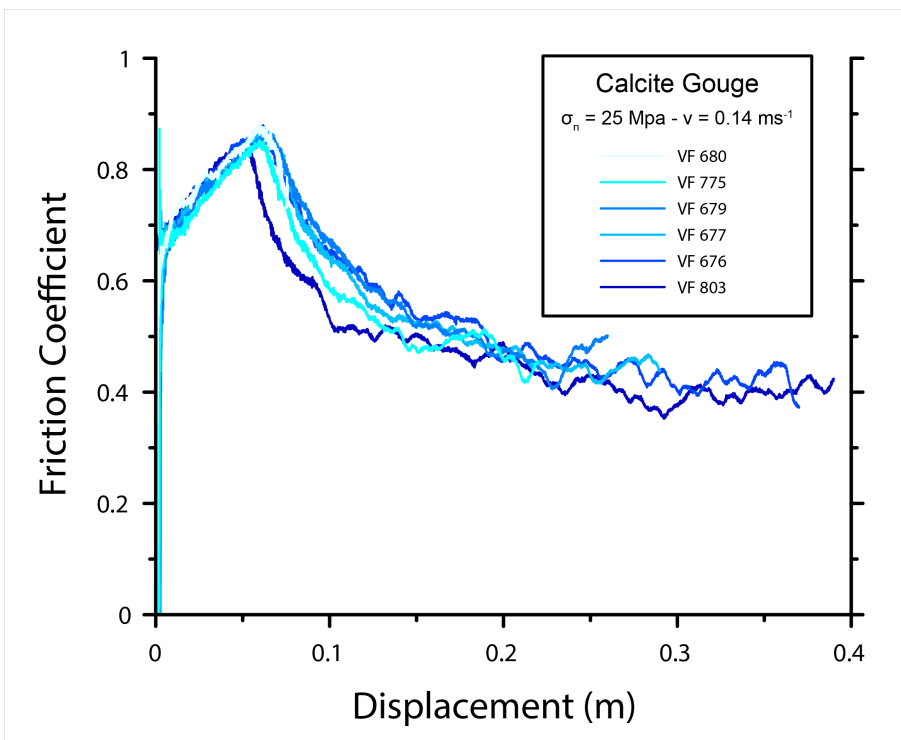


Figure DR4: Friction coefficient curves plotted over displacement for experiments performed at slip rate of 0.14 ms^{-1} .

Axial shortening (ΔW) of the sample occurs during the application of the vertical, normal load. This shortening value depends on the normal load applied, and at $\sigma_n = 25$ MPa it is on average ~ 0.5 mm. This shortening is due to the reduction in porosity that occurs under static conditions, i.e. before any shear motion is imposed to the sample. After the onset of shearing, less than 0.2 mm of shortening occurs during Stage I (Fig. DR5), mostly due to shear-induced compaction. The rate of axial shortening decreases through stage II, and up to 0.15 mm of additional shortening is recorded before the onset of Stage III. During Stage III and IV, the sample slowly shortens until the end of the experiment (1 m of slip), reducing its thickness by less than 0.1 mm. This is probably due to the decrease of porosity induced by sintering outside the PSZ.

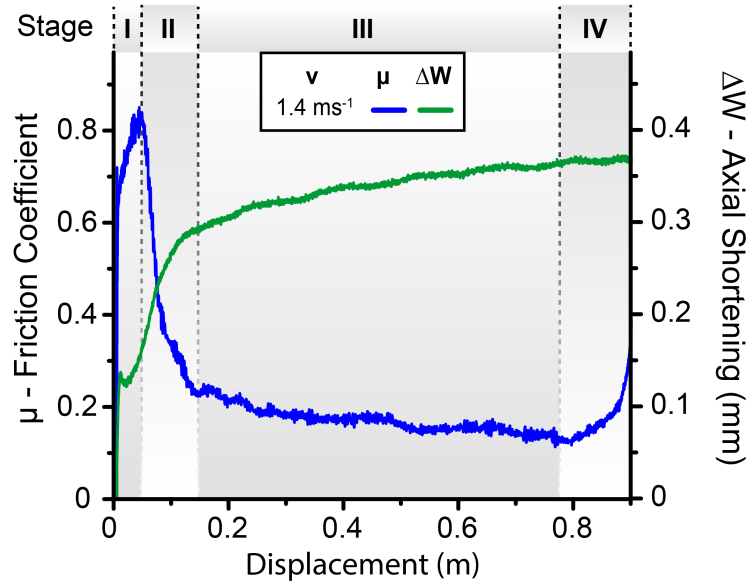


Figure DR5: Representative axial shortening recorded for an experiment run at $\sigma_n = 25$ MPa and $v = 1.4$ ms^{-1} (VF660).

References in DR3.

- De Paola, N., Hirose, T., Mitchell, T., Di Toro, G., Viti, C., and Shimamoto, T., 2011, Fault lubrication and earthquake propagation in thermally unstable rocks: *Geology*, v. 39, p. 35–38.
- Mizoguchi, K., Hirose, T., Shimamoto, T., and Fukuyama, E., 2007, Reconstruction of seismic faulting by high-velocity friction experiments: An example of the 1995 Kobe earthquake: *Geophysical Research Letters*, v. 34, p. L01308.

DR4: Flow Laws

Stage III PSZ microstructure resembles that found in natural (Bestmann et al., 2000; Herwegh and Kunze, 2002) and experimental (Barnhoorn et al., 2004) calcite ultramylonites. From the microstructural and mechanical data it is possible to measure strain rates and temperatures, which are tested with existing flow laws for calcite for both dislocation and grain size sensitive grain boundary sliding (GBS). Following the approach in De Paola *et al.* (2015), a general flow law for creep is used:

$$\dot{\gamma} = A^* \frac{\tau^n}{D^m} e^{\left(-\frac{H}{RT}\right)} \quad (8)$$

where $\dot{\gamma}$ is the strain rate, A^* is the pre-exponential factor, τ is the shear stress, n the stress exponent, D is the grain size and b is the grain size exponent, H is the apparent activation energy for creep, R is the gas constant, T is the absolute temperature.

Table 2 reports the variables used for the two different creep regimes (De Paola *et al.*, 2015 and references therein).

Table 2

Def. Mechanism	A^* ($s^{-1} bar^{-n} \mu m^m$)	n	m	H (kcal mol ⁻¹)	R (kcal K ⁻¹ mol ⁻¹)
Grain Boundary Sliding	$9.55 \cdot 10^4$	1.7	3	51.0	1.987 E-3
Dislocation Creep	$4.6 \cdot 10^{-2}$	4.7	0	71.0	

As discussed in detail in De Paola et al. (2015), the grain size in the PSZ in the post-mortem microstructures is not fully representative of the dynamic values during deformation, due to grain growth by static recrystallization during the cooling stage after the experiment. Flow stress values were therefore calculated for a range of grain sizes (0.10 – 0.01 μm), which are equal or smaller than those observed in the PSZ. Our calculated flow stresses are of the same order of magnitude than those measured during the experiments run at 1 ms^{-1} and 0.14 ms^{-1} (Fig. DR6A and DR6B, respectively).

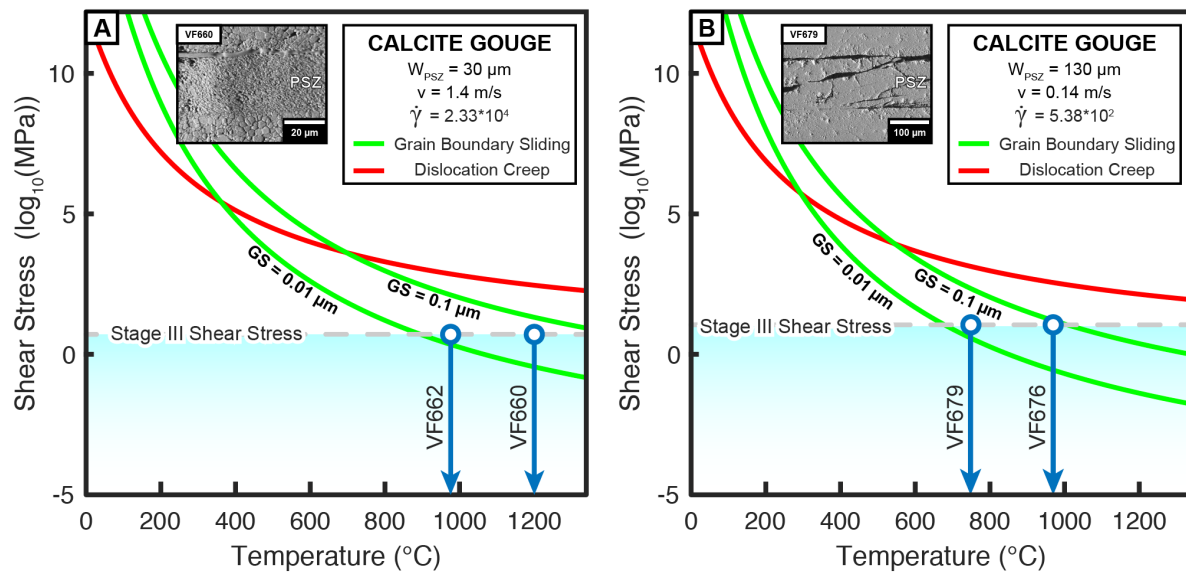


Figure DR6: Predicted flow stress with temperature for grain size sensitive grain boundary sliding (GBS, green curves) and dislocation creep (red curves), calculated using the data from experiments performed at 1.4 ms^{-1} (A) and 0.14 ms^{-1} (B). The flow stress of GBS, unlike in the case of dislocation creep, is affected by the grain size. The flow stress and temperature measured for representative experiments are compatible with those predicted for GBS using a range of grain size between $0.01 \mu m$ and $0.1 \mu m$.

References in DR4.

- Barnhoorn, A., Bystricky, M., Burlini, L., and Kunze, K., 2004, The role of recrystallisation on the deformation behaviour of calcite rocks: large strain torsion experiments on Carrara marble: *Journal of Structural Geology*, v. 26, p. 885–903.
- Bestmann, M., Kunze, K., and Matthews, A., 2000, Evolution of a calcite marble shear zone complex on Thassos Island, Greece: microstructural and textural fabrics and their kinematic significance: *Journal of Structural Geology*, v. 22, p. 1789–1807.
- De Paola, N., Holdsworth, R.E., Viti, C., Colletini, C., and Bullock, R., 2015, Can grain size sensitive flow lubricate faults during the initial stages of earthquake propagation? *Earth and Planetary Science Letters*, v. 431, p. 48–58, doi: 10.1016/j.epsl.2015.09.002.
- Herwegh, M., and Kunze, K., 2002, The influence of nano-scale second-phase particles on deformation of fine grained calcite mylonites: *Journal of Structural Geology*, v. 24, p. 1463–1478.

DR5: Microstructures

Samples recovered after the onset of weakening (Stage II and III) easily split along mirror-like surfaces. Careful recovery is required to obtain the full sample thickness for microstructural analysis.

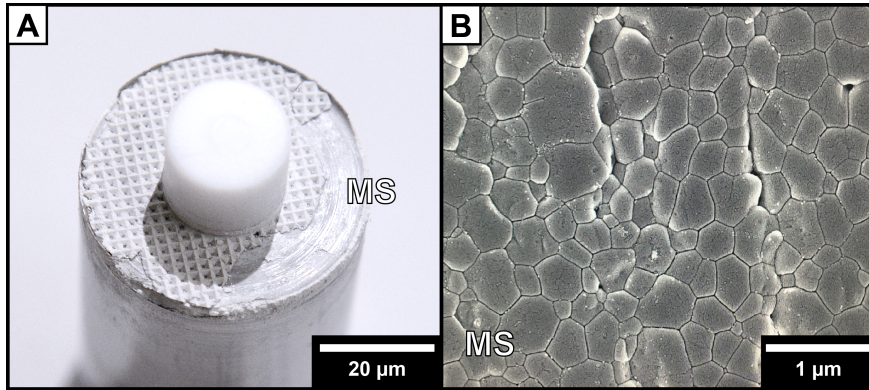


Figure DR7: A) Sample of calcite gouge sheared at $\sigma_n = 25$ MPa and $v = 1.4$ ms⁻¹ up to stage III (1 m of slip), still mounted on the bottom cylinder after unloading and removal from the machine. Part of the sample (left hand side) has split revealing a shiny mirror-like surface (MS). Concentric grooves are visible on the MS. Successful recovery of the full sample thickness is possible where the imprint of the top cylinder (crosshatch pattern) is visible. B) Back scattered electron image of the MS. The shininess of the MSs (Fig. DR7A) is due to their smoothness, which is caused by the coating with sintered (porosity-free) submicron sized grains (see also De Paola et al., 2013 and references therein).

Samples share the same evolution in microstructural architecture but the characteristic dimensions of their microstructures (e.g. grainsize, slip zone thickness) seem to vary with different slip rates. Hence, reported measures in the paper are referred to samples sheared at $v = 1.4$ ms⁻¹.

Here are reported the enlarged back scattered (BSD) and forward scattered (FSD) electron images used to compose fig. 2 and 3 in the paper.

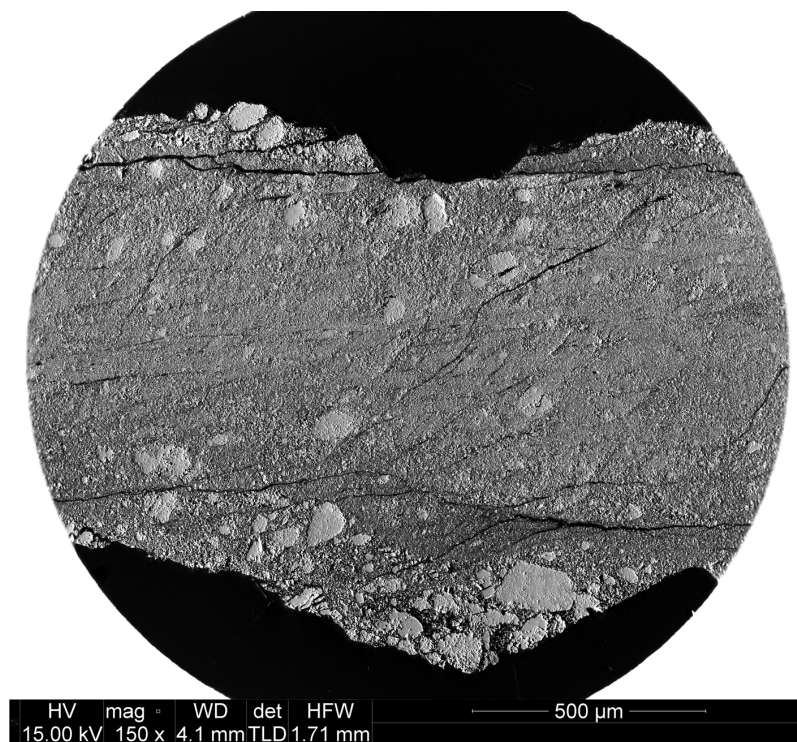


Figure DR8: Original BSD image of fig. 2A in the paper (stage I). VF 666, $v = 1.4$ ms⁻¹, $\delta = 0.04$ m.

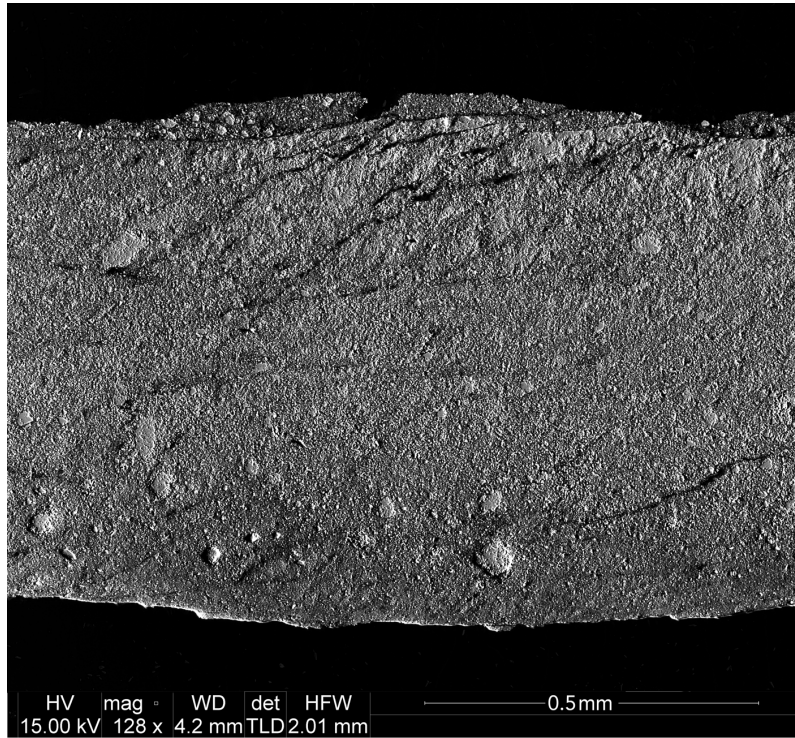


Figure DR9: Original BSD image of fig. 2B in the paper (stage II). VF 664, $v = 1.4 \text{ ms}^{-1}$, $\delta = 0.07 \text{ m}$.

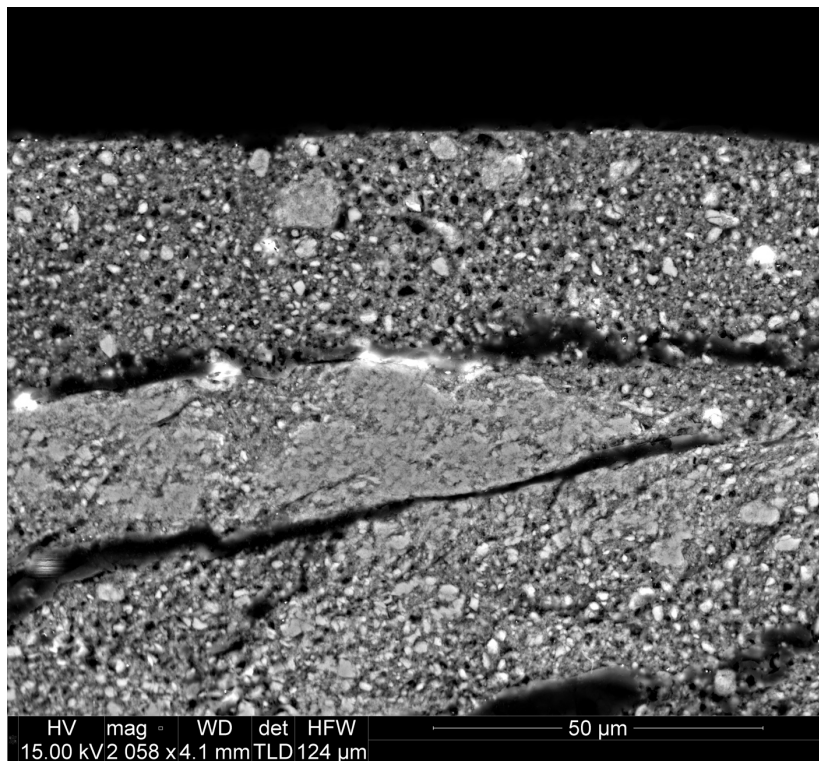


Figure DR10: Original BSD image of fig. 2C in the paper (close up of fig. 2b, PSZ, stage II). VF 664, $v = 1.4 \text{ ms}^{-1}$, $\delta = 0.07 \text{ m}$.

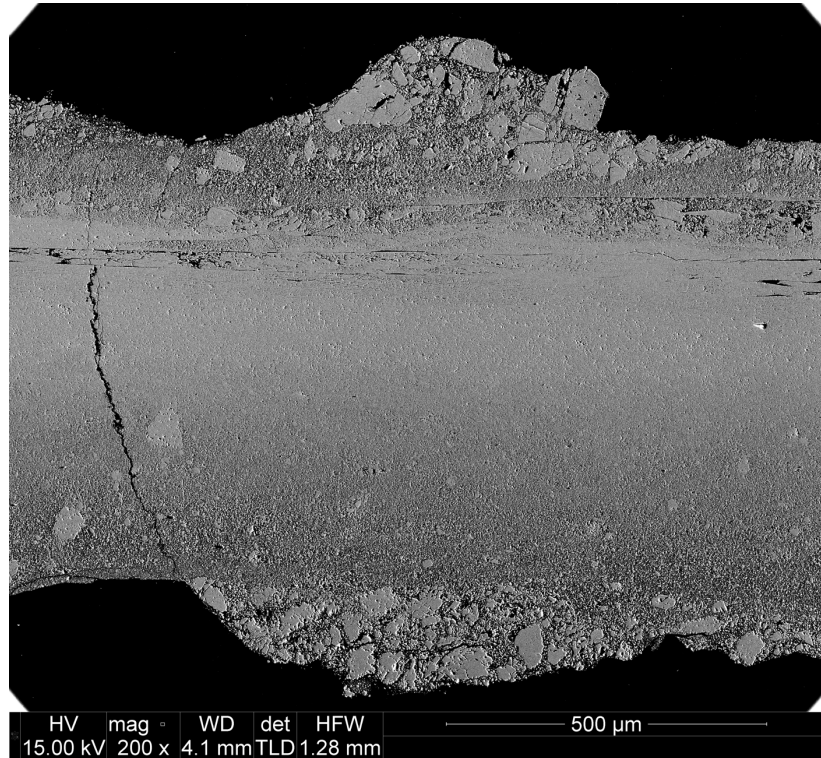


Figure DR11: Original BSD image of fig. 2D in the paper (stage III-IV). VF 660, $v = 1.4 \text{ ms}^{-1}$, $\delta = 0.9 \text{ m}$.

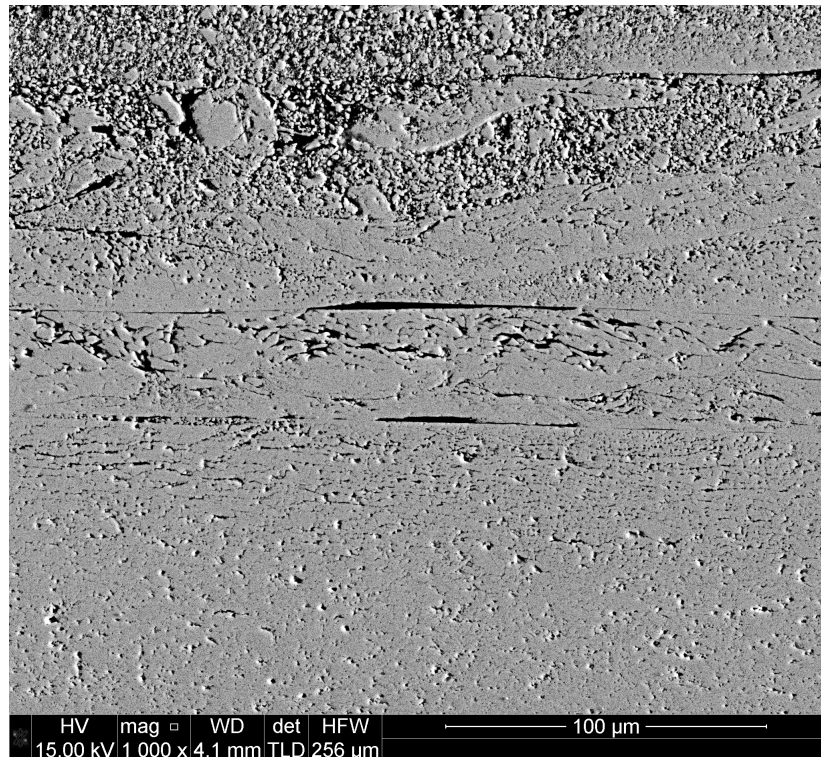


Figure DR12: Original BSD image of fig. 3A in the paper (close up of fig. 2d, PSZ, stage III-IV). VF 660, $v = 1.4 \text{ ms}^{-1}$, $\delta = 0.9 \text{ m}$.

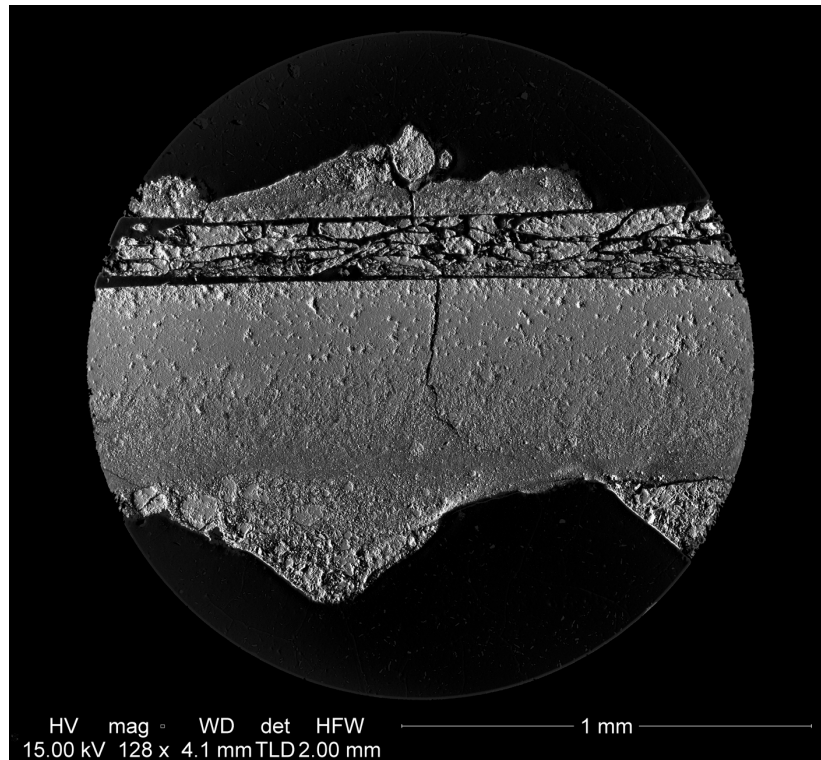


Figure DR13: Original BSD image of fig. 2E in the paper (stage III-IV). VF 675, $v = 1.4 \text{ ms}^{-1}$, $\delta = 0.23 \text{ m}$.

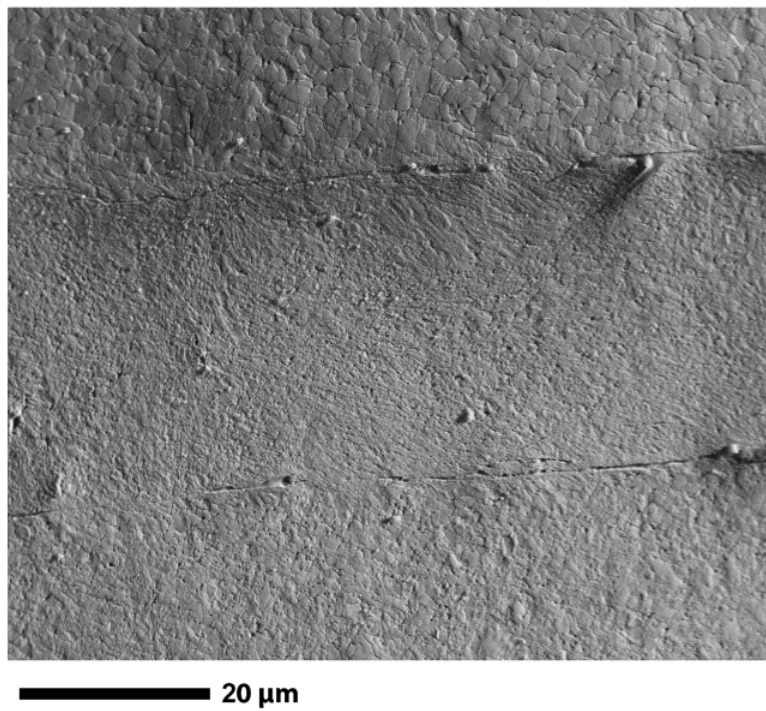


Figure DR14: FSD image of early stage III PSZ (stage III-IV). VF 662, $v = 1.4 \text{ ms}^{-1}$, $\delta = 0.26 \text{ m}$.



Figure DR15: FSD image of stage III PSZ (stage III-IV). VF 660, $v=1.4 \text{ ms}^{-1}$, $\delta = 0.9 \text{ m}$.

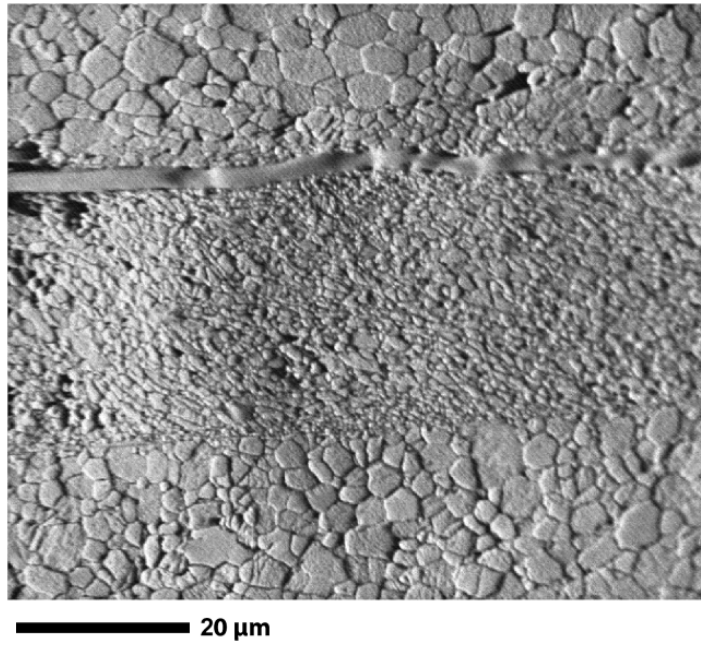


Figure DR16: Original FSD image of Fig. 3B in the paper (stage III-IV). VF 660, $v = 1.4 \text{ ms}^{-1}$, $\delta = 0.9 \text{ m}$.

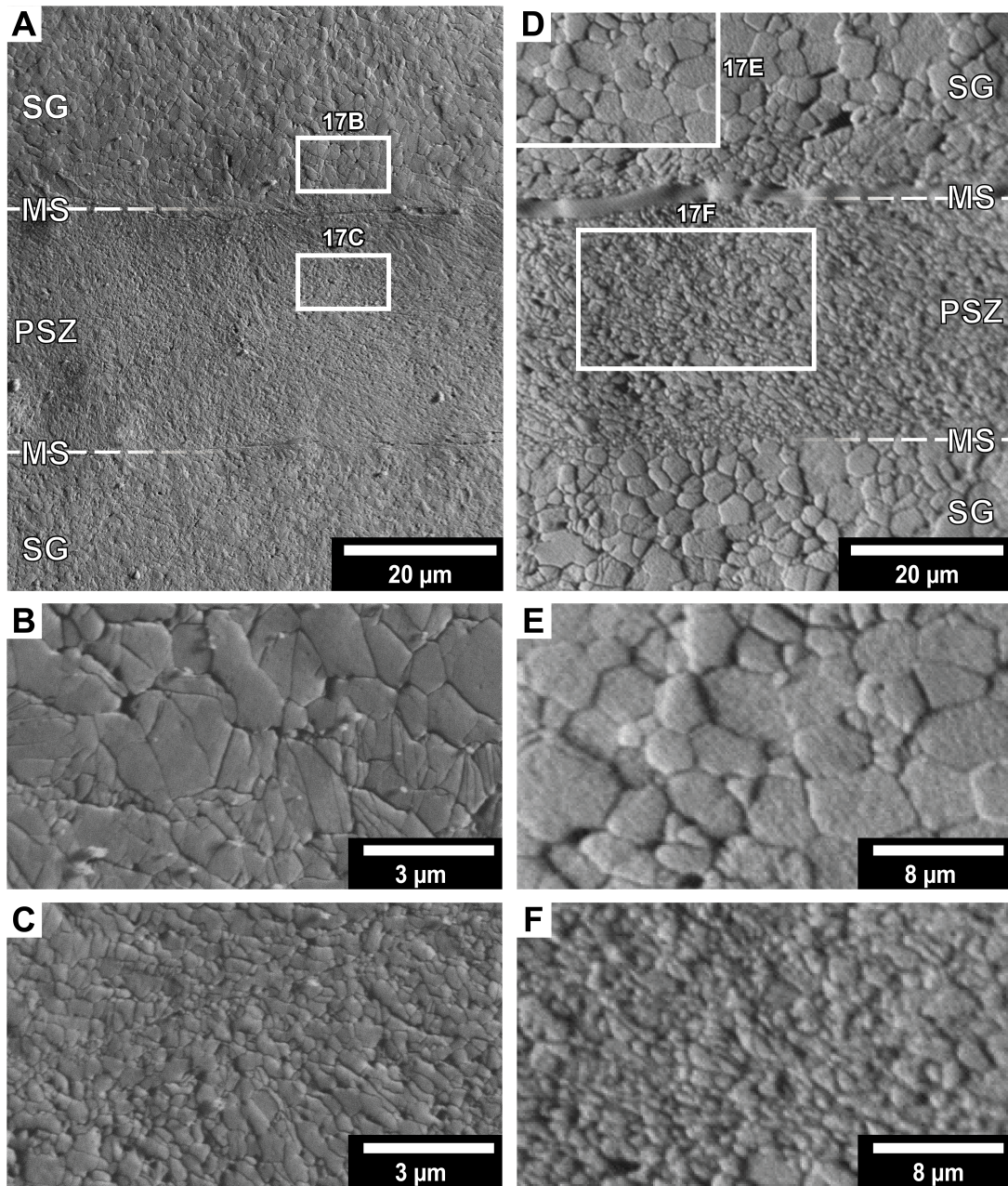


Figure DR17: Grain size comparison between FSD images of sample VF662 ($v= 1.4 \text{ ms}^{-1}$, $\delta = 0.26 \text{ m}$, Fig. DR14) and VF660 ($v= 1.4 \text{ ms}^{-1}$, $\delta = 0.9 \text{ m}$ Fig. DR16). A) early stage III PSZ; B) close up of early stage III grains in the SG close to PSZ; C) close up of early stage III grains in the PSZ; D) stage III PSZ; E) close up of stage III grains in the SG close to PSZ; F) close up of stage III grains in the PSZ.

References in DR5.

De Paola, N., 2013, Nano-powder coating can make fault surfaces smooth and shiny: Implications for fault mechanics? *Geology*, v. 41, p. 719–720.